ASCE

Dynamic Tensile Mechanical Properties and Fracture Characteristics of Water-Saturated Sandstone under the Freezing Effect

Gang Lin, Ph.D.[1]; Ming Li[2]; Yanlong Chen[3]; Jiazhi Zhang, Ph.D.[4]; Izhar Mithal Jiskani, Ph.D.[5]; Dao Viet Doan[6]; and Lei Xu[7]

Abstract: Dynamic tensile mechanical characteristics of coal-rock mass under the freezing effect are an important subject that is supposed to be studied during the blasting of open-pit coal mines in Northwest China. In this study, the split Hopkinson pressure bar (SHPB) test system was used to perform dynamic Brazilian disc tests on saturated sandstone at normal temperature (25°C) and negative temperatures (−5°C, −10°C, −20°C, and −30°C). The high-speed failure process, macrofracture roughness and mesofracture morphologies of the samples were observed at different temperatures. The experimental results showed that the dynamic tensile strength of sandstone first increased and then decreased with the decrease of freezing temperature. In addition, a statistical model of the variation of sandstone tensile strength under the effect of temperature and loading rate was established. At different temperatures, all samples underwent the process of crack initiation from the center and then the main cracks penetrated the sample. At room temperature, a large number of secondary cracks formed at both ends of the samples and gradually merged with main cracks that do not occur at low temperatures. The fracture roughness of the sample at normal temperature was significantly greater than that at freezing temperatures, and there were no obvious rules of the roughness of fracture surfaces at different freezing temperatures. In the end, the change in the macroroughness of the fracture surface was explained by the brittle–ductile transition of the mesofracture morphologies of the sandstone samples at different temperatures. **DOI: 10.1061/(ASCE)GM.1943-5622.0001999**

Author keywords: Freezing effect; Load rate; Dynamic tensile strength; Roughness; Mesofracture morphology.

Introduction

There are abundant coal resources in Xinjiang and Inner Mongolia regions of China, and more than 40% of coal resources have open-pit mining conditions. Most open-pit mines adopt the loose blasting method, and the explosive blasting process has a significant impact dynamic load on coal-rock mass. It could provide the basis for the optimal design of blasting parameters based on dynamic mechanical properties and failure characteristics of coal-rock mass. More significantly, compared with open-pit mining in Yunnan and Shanxi Provinces, low temperature is an important environmental influencing factor in Xinjiang and Inner Mongolia. In the process of loose blasting of the coal seam, the mechanical response characteristics of coal-rock mass at low temperatures are significantly different from those at normal temperature (Inada and Yokota 1984; Park et al. 2004; Ulrich and Darling 2001). For example, Beitashan Pasture Coal Mine in Xinjiang (Fig. 1) was under 0°C for nearly 200 days of the whole year. How to design coal seam blasting parameters at low temperatures is an important issue for safe and efficient production. In addition, coal-rock media are typical materials with compressive strength much greater than the tensile strength, and its fracture failure is mostly a tensile failure. Therefore, it is important to study dynamic tensile mechanical properties of coal-rock mass under the effect of freezing on coal seam mining and slope stability control in Xinjiang and Inner Mongolia.

In a low-temperature environment, the stability of the geotechnical structure is significantly affected by the freezing damage, such as road boiling caused by frost heaving (Lai et al. 2012) and instability of the slope caused by freezing and thawing (Korshunov et al. 2016; Li et al. 2018b; Luo et al. 2015). The change in the mechanical properties of rock under the effect of low temperatures is the fundamental cause of structural instability. At present, the research results for rock static mechanical properties under low temperature are abundant, including the variation characteristics of compressive strength (Yamabe and Neaupane 2001), fracture toughness (Dwivedi et al. 2000), and tensile strength (Aoki et al. 1990). With the development of experimental techniques and test methods, in recent years, some scholars have focused on the

[1]School of Mechanics and Civil Engineering, China Univ. of Mining and Technology, Xuzhou 221116, China. Email: ts18030025a31@cumt.edu.cn

[2]Associate Professor, State Key Laboratory for Geomechanics and Deep Underground Engineering, China Univ. of Mining and Technology, Xuzhou 221116, China (corresponding author). Email: mingl@cumt.edu.cn

[3]Associate Professor, State Key Laboratory for Geomechanics and Deep Underground Engineering, China Univ. of Mining and Technology, Xuzhou 221116, China. Email: chenyanlong@cumt.edu.cn

[4]School of Mechanics and Civil Engineering, China Univ. of Mining and Technology, Xuzhou 221116, China. Email: ts19030220p31@cumt.edu.cn

[5]School of Mines, China Univ. of Mining and Technology, Xuzhou 221116, China. ORCID: https://orcid.org/0000-0002-3220-8880. Email: imjiskani@hotmail.com

[6]Lecturer, Dept. of Underground and Mining Construction, Hanoi Univ. of Mining and Geology, 100803 Hanoi, Vietnam. Email: daovietdoan@gmail.com

[7]Master, School of Mechanics and Civil Engineering, China Univ. of Mining and Technology, Xuzhou 221116, China. Email: xlei@cumt.edu.cn

Note. This manuscript was submitted on December 26, 2019; approved on December 6, 2020; published online on February 23, 2021. Discussion period open until July 23, 2021; separate discussions must be submitted for individual papers. This paper is part of the ***International Journal of Geomechanics***, © ASCE, ISSN 1532-3641.

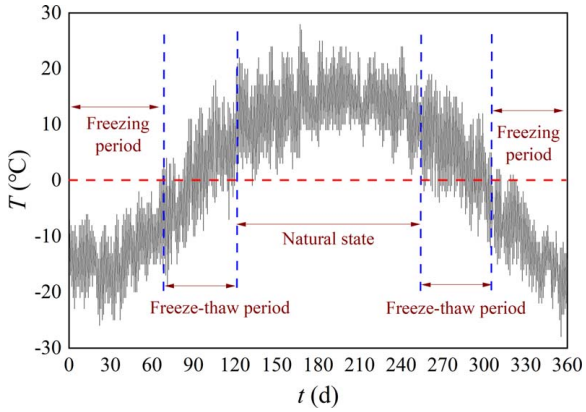

Fig. 1. Temperature variation characteristics of Beitashan Pasture Coal Mine in Xinjiang, China, in 2018 (north latitude 44°59′20″–45°33′20″ and east longitude 90°16′45″–91°11′48″).

experimental study of dynamic mechanical properties of rock at low temperatures. Li et al. (2018a) carried out the dynamic load test of sandstone after the freeze–thaw cycle. They combined with nuclear magnetic resonance technology to analyze the change in the pore structure after the freeze–thaw cycle and explained the degradation of dynamic compression mechanical strength. Liu et al. (2018) used nuclear magnetic resonance to detect changes in the pore structure and explained the degree of deterioration of the dynamic tensile strength of granite after several freeze–thaw cycles. Chen et al. (2019) studied the effect of different temperatures on the dynamic compressive strength of sandstone during eight freeze–thaw cycles and pointed out that the lower the temperature of the freeze–thaw cycle, the more severe the dynamic strength degradation of sandstone. Wang et al. (2017) proposed an analysis method for the damage evolution process under dynamic loading after freeze–thaw cycles based on the energy change in the process of dynamic failure of red sandstone. Wang et al. (2016) also proposed to predict the strength change of sedimentary rocks after the freeze–thaw cycle. The current research studies on the coupling of low temperature and dynamic load mainly focus on the deterioration of dynamic mechanical properties of rocks after freeze–thaw cycles. However, there are few research studies on the dynamic loading of rocks under freezing conditions. Renliang et al. (2019) conducted a dynamic uniaxial compression test of red sandstone at −15°C and established a constitutive model to predict the change of compressive strength at low temperatures. Weng et al. (2019) conducted a dynamic uniaxial compression test of siltstone at −50°C to 25°C to study the energy dissipation density during the dynamic failure process at different low temperatures. It was found that with the decrease of freezing temperature, the energy dissipation density first increased and then decreased and the energy dissipation density reached its peak at −30°C. Yang et al. (2019) conducted dynamic uniaxial compression tests at −40°C to 25°C for sandstone, marble, and granite and introduced the concept of temperature influence factor, gave the influence degree of different freezing temperatures on three types of rocks, and made some explanations on the mechanism of rock strength variation at different freezing temperatures. At present, the research achievements in this field are limited, and the few existing research achievements are only the dynamic compressive properties of rocks under the freezing effect.

The testing methods of dynamic tensile properties of rock mainly include the direct tensile test and the indirect tensile test. Due to the low success rate and the complex operation method of the dynamic direct tensile test, it was seldom used in previous studies. However, the Brazilian disc (BD) as one kind of dynamic indirect tensile test method is recommended by the ISRM because of its simple operation and convenient sample processing (Xia and Yao 2015; Zhou et al. 2012). Numerical simulation was also used to prove the validity of the dynamic BD tests (Hughes et al. 1993; Zhu and Tang 2006). Dynamic BD tests have been widely used to measure the dynamic mechanical properties of rock by scholars. Yin et al. (2015) conducted a BD test on Laurentian granite after high-temperature treatment to explore the change laws of rock tensile strength at treatment temperatures. Zhou and Zhu (2017) carried out a dynamic and static BD test and verified the consistency of the splitting tensile process and the results of natural rocks and artificial rocks printed with the transparent resin. Zhou et al. (2018) studied the functional relationship between the attenuation degree of the dynamic tensile strength of rocks and times of dry and wet cycles. Besides, in terms of energy of dynamic tensile failure, Ping et al. (2013) concluded that both the dynamic tensile strength and the absorbed energy of sandstone during the failure process increased approximately logarithmically with the increase of the average strain rate. Gong and Hu (2020) introduced the fracture failure patterns of yellow sandstone at different incident energies. Liu et al. (2020) pointed out that the dynamic tensile strength and fracture energy of the ore would change with its grade. In recent years, some new technologies such as digital image correlation and holographic interferometry have been applied to the measurement of the strain field on the surface of samples in the dynamic BD test and abundant research results have been obtained (Ai et al. 2020; Heard et al. 2018; Xing et al. 2019; Zhang and Zhao 2014). Currently, some scholars have also begun to conduct Brazilian splitting tests of rocks under prestress, such as initial tensile stress (Pei et al. 2020; Wu et al. 2015) and initial hydrostatic confining pressure (Wang et al. 2019; Wu et al. 2016). In short, the dynamic BD test has been widely accepted as a reliable method to measure the tensile strength of rocks. It can be inferred from the aforementioned studies that the dynamic BD test is suitable to test the dynamic tensile mechanical properties of rocks at low temperatures.

In this paper, considering the mining of Beitashan Pasture Coal Mine during the freezing period, the dynamic splitting tensile test of saturated sandstones at normal temperature (25°C) and freezing (−5°C, −10°C, −20°C, and −30°C) was carried out with the SHPB test device. The splitting tensile test was conducted to investigate the variation of the tensile strength of saturated sandstone with freezing temperature and loading rate. Based on the experimental data, a regression model was established to predict the change in tensile strength with freezing temperature and loading rate. This research also further studied the influence of different freezing temperatures on the dynamic failure process of samples and macroscopic fracture characteristics. In addition, the reasons for the variation of the macroscopic fracture characteristics under different freezing temperatures were given from the mesoscopic perspective. The results of the research can provide theoretical support for the parameter design of blast engineering in the cold region.

Samples Preparation and Test Method

Samples Preparation

Rock samples used in this test were slope sandstone from Beitashan Pasture Open-pit Coal Mine in Xinjiang, China. The material was tested by X-ray diffraction (Fig. 2): quartz (65.5%), muscovite (28.7%), kaolinite (3.4%), boron muscovite (1.5%), and

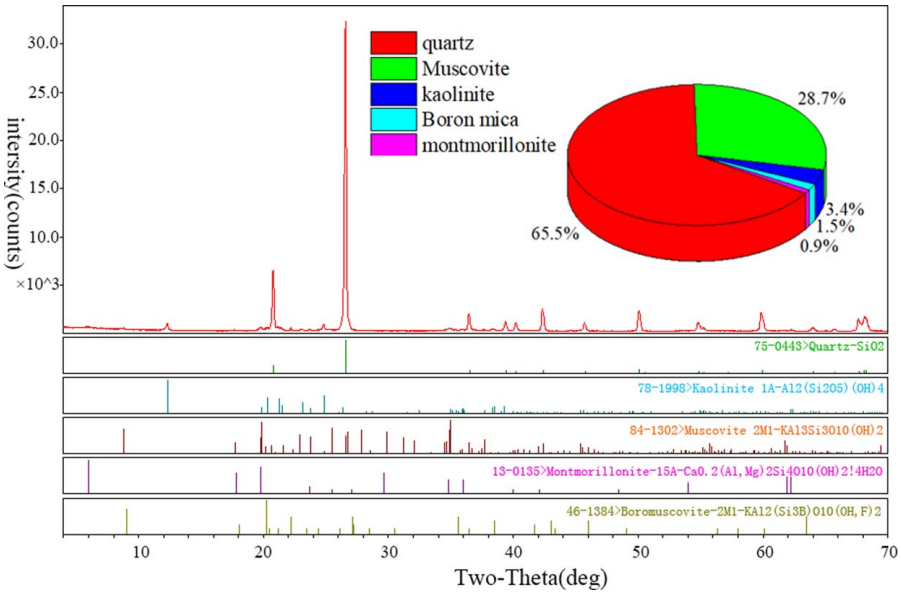

Fig. 2. X-ray diffraction test results of rock sample materials.

Table 1. Basic physical and mechanical properties of sandstone samples (size: diameter of 50 mm, height of 100 mm)

Samples	ρ (kg · m^{-3})	σ_c (MPa)	E (GPa)	v (km · s^{-1})
1 #	2,282	45.34	4.36	2.817
2 #	2,283	46.27	4.72	2.805
3 #	2,285	43.81	4.68	2.836
Average value	2,283	45.14	4.59	2.819

montmorillonite (0.9%). Through the coring, cutting, and grinding work, the rock was processed into cylindrical samples with a diameter of 50 mm and a height of 25 mm. The rock acoustic wave instrument was used to test the acoustic wave velocity of the samples, and the samples with similar wave velocities were selected as the test objects. The basic physical and mechanical properties of samples are shown in Table 1.

Saturated Water Treatment and Freezing Treatment of Samples

Saturated Water Treatment of Samples

According to the relevant recommendations in the ISRM, the water saturation process of the samples was mainly divided into two parts: (1) drying; and (1) water saturation.

1. Drying: The samples were continuously dried at 105°C for 24 h in the DHG9076 electric thermostatic constant-temperature drying oven [Fig. 3(a)]. Then, they were weighed every 1 h until the weight difference between the two times was less than 0.01 g. Next, all the dried samples were taken out and placed into a desiccator. When they were cooled to room temperature, they were sealed with sealed bags.
2. Water saturation: Dried samples were placed into a negative pressure vacuum pumping system to be pumped at a pressure of −0.09 MPa for 6 h [Fig. 3(b)]. Then, water was injected into the sealed tank until all samples were submerged. Finally, the sealed tank was pumped to −0.09 MPa again. Numerous bubbles overflowed from the samples surfaces at the early stage of saturation. The pressure inside the sealed tank was set to atmospheric pressure once no bubble overflowed from the samples surfaces, and the samples remained in the sealed tank for 6 h. After that, the samples were weighted every hour. They were considered to be fully saturated if the difference between the adjacent weights was less than 0.01 g.

Freezing Process of Samples

The freezing process of the saturated samples was realized by the JC-ZDR-5 automatic low-temperature freeze–thaw test machine [Fig. 3(c)] with the controllable temperature range of −50°C–80°C. During the freezing process, the sealed samples were frozen in the freeze–thaw chamber for 48 h. According to the actual annual temperature change of Beitashan Pasture Coal Mine, the test temperature gradient was selected as normal temperature (25°C), −5°C, −10°C, −20°C, and −30°C. After samples were taken out of the freeze–thaw chamber, the dynamic tensile test was completed within 2 min to ensure that they were still frozen during the dynamic loading test.

It should be noted that the water saturated and freezing process of samples were carried out in the State Key Laboratory for Geomechanics and Deep Underground Engineering, China University of Mining and Technology. The equipment used in the test process all belonged to this laboratory.

Dynamic Splitting Tensile Test and Process

Experimental procedure

The dynamic tensile loading test of freezing sandstone was carried out by using a 50-mm-diameter split Hopkinson pressure bar (SHPB) system, and the Brazilian Disk test was adopted. Fig. 4 shows a schematic illustration of the SHPB test system, which is from the State Key Laboratory for Geomechanics and Deep Underground Engineering. It mainly consists of a striker, an incident bar, and a transmitted bar, which are made of high-strength spring steel. During the test, the high-pressure nitrogen inside the gas gun pushes the striker to impact the incident bar. A stress pulse (incident wave) is generated, and then it is transmitted along the incident bar to the sample. A part of the stress pulse is reflected back into the incident bar at the contact end of the incident bar and the samples and forms a reflected wave. The other part waves are refracted and reflected multiple times in the sample and then transmitted into the transmission bar to form a transmitted wave.

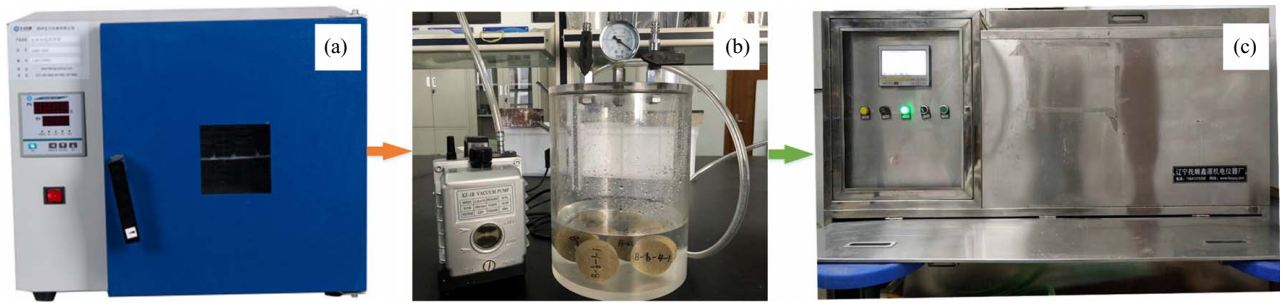

Fig. 3. Sample processing: (a) drying (equipment: DHG9076 electric thermostatic constant-temperature drying oven); (b) water saturation (equipment: negative pressure vacuum pumping system); and (c) freeze processing (equipment: JC-ZDR-5 automatic low-temperature freeze–thaw test machine. (Images by Gang Lin.)

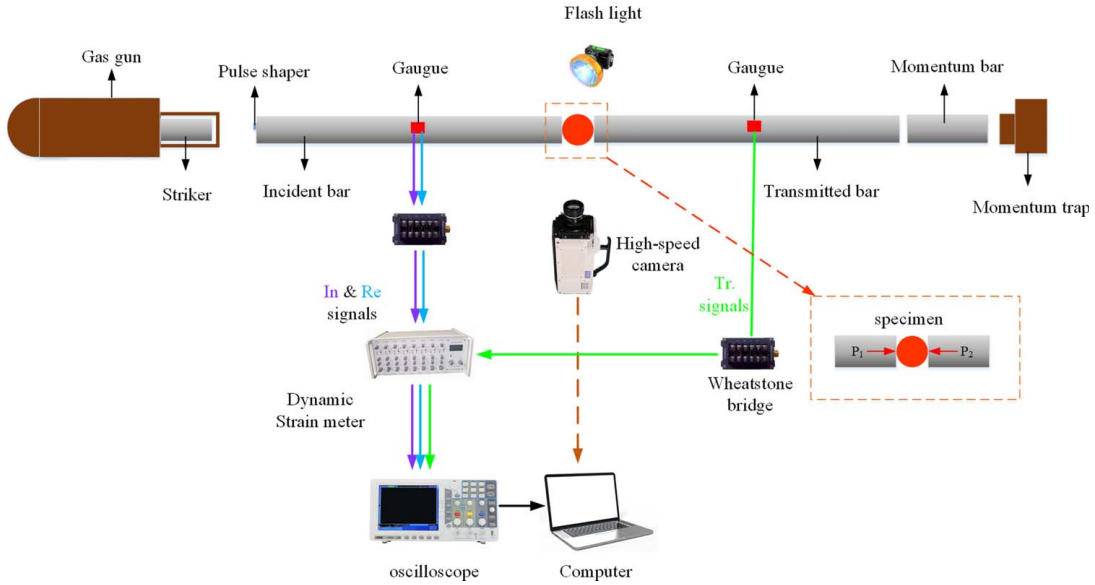

Fig. 4. Split Hopkinson pressure bar system.

The strain signals in the incident and transmitted bars are transmitted through the strain gauges to the dynamic strainmeter. The dynamic failure process of the sample is captured by a high-speed camera.

Test principle and test waveform

According to the elastic bar theory (Kolsky 1949; Kolsky 1953), the loading forces P_1 and P_2 at both ends of the sample (labeled in Fig. 4) can be calculated by the following equation:

$$\begin{cases} P_1 = AE(\varepsilon_i + \varepsilon_r) \\ P_2 = AE\varepsilon_t \end{cases} \quad (1)$$

where A = cross-sectional area of the pressure bar, m^2; E = elastic module of the pressure bar, 210 GPa; and ε_i, ε_r, and ε_t are incident, reflected, and transmitted signals, respectively.

The force equilibrium at both ends of the sample is a precondition for the success of the dynamic Brazilian splitting test (Li et al. 2017). A C1100 copper slice with a diameter of 5 mm and a thickness of 1 mm was attached to the loading end of the incident bar as a pulse shaper (Chen et al. 2003; Yin et al. 2015) so that the stress wave had a longer *rising edge* during the test, which could make the sample reach force equilibrium before its failure. Fig. 5 shows the force equilibrium verification of the specific test, and it can be seen that the force at the incident end (P_1) and the force at the transmitting end (P_2) are basically coincident. The test result satisfies the force balance condition well, which is $P_1 = P_2$. According to P_2 in Eq. (1), the tensile strength of the sample can be calculated as follows (ISRM 1978; Zhou et al. 2012):

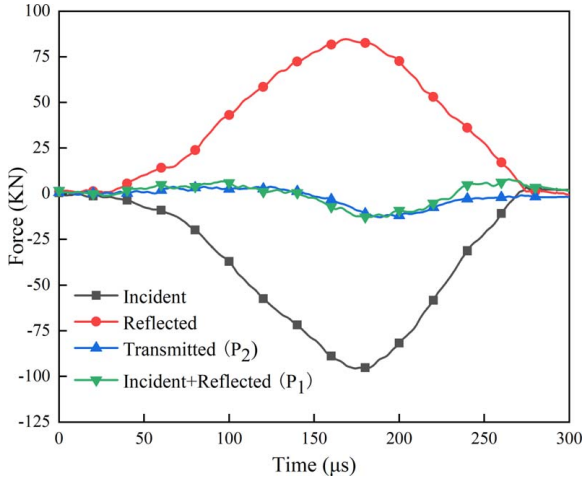

Fig. 5. Dynamic force equilibrium check for a typical test with pulse shaper.

$$\sigma_t = \frac{2P_{2\max}}{\pi DB} \tag{2}$$

where D = diameter of the sample; and B = thickness of the sample.

Determination of Loading Rate

According to the dynamic tensile strength test method for rock materials by the ISRM (Zhou et al. 2012), the slope of the prepeak linear segment in the stress loading history curve of the sample is defined as the loading rate $\dot{\sigma}_t$. Fig. 6 shows the stress loading history curve of a sample. It can be seen that there is an approximately linear increasing segment lasting from 25 to 50 μs, and the slope of this segment is 269.6 GPa/s, which is the loading rate for this test. Many studies showed that the dynamic tensile strength had exhibited significant loading rate correlation in dynamic Brazilian splitting tests of rock-like materials (Dai et al. 2010a, b; Zhou et al. 2018).

Variation of Dynamic Tensile Strength and Its Prediction

Variation Law of Dynamic Tensile Strength

The tensile strength of sandstone under different temperatures and loading rates was obtained, as shown in Table 2. In Table 2, σ_t is the tensile strength of sandstone, MPa; $\dot{\sigma}_t$ is the loading rate, GPa/s. Some data of tensile strength were rejected because they did not satisfy the force equilibrium. According to the experimental results, the change curves of dynamic tensile strength were drawn, as shown in Fig. 7. Fig. 7(a) shows that the splitting tensile strength of saturated sandstone gradually increased with the loading rate and all of them showed significant loading rate correlation at different temperatures. Five data with loading rate ranging from 240 to 250 GPa/s were selected from Fig. 7(a) to study variation characteristics of tensile strength at different freezing temperatures with the same loading rates, as shown in Fig. 7(b). Fig. 7(b) shows that the change process of strength can be divided into three stages. During the change process from normal temperature (25°C) to −5°C (Stage 1), the tensile strength of sandstone increased from 12.3 to 15.2 MPa, an increase of 23.58%. From −5°C to −20°C (Stage 2), the tensile strength increased from 15.2 to 18.7 MPa, an increase of 23.03%. From −20°C to −30°C (Stage 3), the tensile strength began to deteriorate, from 18.7 to 17.1 MPa, a decrease of 8.56%.

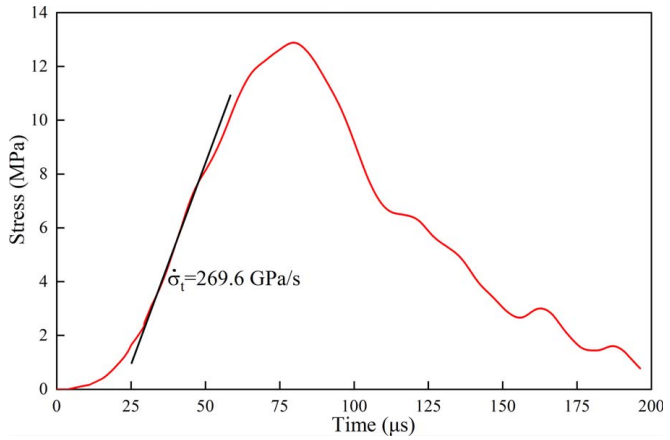

Fig. 6. Stress loading history curve and determination of loading rate.

The main reasons for the change of tensile strength of sandstone with freezing temperature are given in the following.

At normal temperature, the tensile strength of saturated sandstone is significantly lower than that of frozen sandstone for two main reasons. First, the water in pores and cracks of sandstone is frozen to ice, and the volume expands, so the space of pores and cracks of sandstone is filled, which makes the internal structure of the sample more compact. The second reason is that the water in the cement condenses into ice, which strengthens the cohesive force between the grains and improves the dynamic tensile strength of the sandstone (Liu et al. 2017).

In Stage 2, the strength of saturated sandstone increased with the decrease in freezing temperature. There were mainly two viewpoints for the mechanism. One viewpoint is that the cement and mineral particles in the sandstone gradually shrink with the decrease of the freezing temperature and the volume of the ice crystal expands, which makes the internal material components of the sandstone squeeze tightly together. These cause pores to shrink and microcracks close in the original structure. Thus, the structure of sandstone gradually reaches a more compact state, which results in an increase in the tensile strength of the rock (Yang et al. 2019). The other viewpoint is that the freezing temperature of the pore water is related to the pore size. In particular, a smaller pore size yields a lower freezing point. As the freezing temperature decreases, more and more pore water in small pores condense into

Table 2. Test results of dynamic tensile test

	25°C		−5°C		−10°C		−20°C		−30°C	
No.	$\dot{\sigma}_t$ (GP/s)	σ_t (MPa)	$\dot{\sigma}_t$ (GP/s)	σ_t (MPa)	$\dot{\sigma}_t$ (GP/s)	σ_t (MPa)	$\dot{\sigma}_t$ (GP/s)	σ_t (MPa)	$\dot{\sigma}_t$ (GP/s)	σ_t (MPa)
1	51.1	7.1	75.6	9.9	—	—	82.1	11.4	88.8	10.9
2	54.6	6.9	75.7	9.4	—	—	115.3	13.6	118.0	12.4
3	79.3	8.2	113.2	11.1	102.5	11.9	119.7	13.6	135.6	12.7
4	134.8	9.6	—	—	136.7	14.3	175.9	16.3	164.7	14.4
5	146.8	10.3	208.8	15.0	139.7	13.5	183.1	16.4	181.5	13.8
6	151.8	10.4	241.0	15.2	146.7	14.0	189.8	16.4	207.3	15.4
7	170.0	11.2	287.2	17.0	163.7	14.2	206.0	17.0	249.3	17.1
8	175.2	11.4	297.0	16.2	193.4	15.9	215.0	17.8	—	—
9	186.4	11.0	297.0	16.7	242.1	17.7	244.3	18.7	322.3	19.0
10	197.9	11.2	324.0	17.4	256.7	17.8	250.2	19.0	335.5	18.9
11	240.2	12.3	329.7	18.0	320.0	19.7	282.7	19.3	336.2	19.2
12	269.6	13.1	414.0	19.2	352.1	20.6	314.7	20.8	362.4	19.7
13	297.9	13.4	419.6	19.8	394.6	22.4	322.4	20.8	400.4	20.7
14	421.3	16.0	445.7	20.2	421.9	22.3	425.7	23.4	419.5	20.8
15	453.7	16.2	467.7	20.5	475.7	23.8	—	—	485.4	22.2

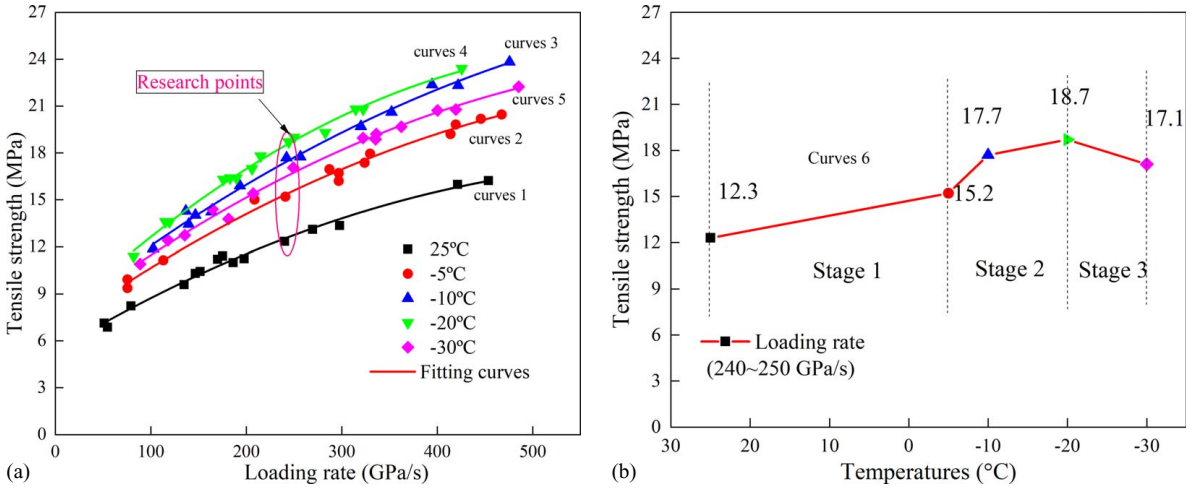

Fig. 7. Change relationships of dynamic tensile strength: (a) change relationships between dynamic tensile strength and loading rates; and (b) dynamic tensile strength at loading rates of 240–250 GPa/s.

Table 3. Fitted tensile strength under different temperatures and loading rates

	Loading rates (GPa/s)				
Temperatures (°C)	100	200	300	400	500
25	8.772	11.638	13.948	15.702	16.900
−5	10.632	14.053	16.888	19.137	20.800
−10	12.123	16.071	19.051	22.263	24.507
−20	12.645	17.006	20.408	22.850	24.333
−30	11.442	15.090	18.104	20.484	22.229

ice, which will gradually strengthen the rock structure, so that the strength of the rock gradually increases with the decrease of freezing temperature (Chen et al. 2004; Weng et al. 2019).

The sudden decrease of rock strength in Stage 3 is because after the pore water is completely condensed into ice, there is a 9% volume expansion. However, the rock skeleton limits the expansion of the ice volume, which causes tensile and shear stresses inside the rock. At this point, some new cracks initiation and propagation can be observed on the rock structure, so the macroscopic tensile strength decreases. In general, the intrinsic mechanism of rock strength change under freezing is a very complicated problem, which might be caused by several factors working together, and more research in this field needs to be done by researchers.

Prediction Model of Tensile Strength under the Effect of Freezing and Strain Rate

Regression analysis is a commonly used method in rock mechanics research, which is often used to establish the empirical relationships between the interrelated mechanical properties of rocks (Azimian and Ajalloeian 2015; Karakul and Ulusay 2013). In this paper, the nonlinear regression method was used to construct the relationship among the dynamic tensile strength σ_t, loading rate $\dot{\sigma}_t$, and freezing temperature T of sandstone. Owing to the dispersion of loading rates in the actual tests, it is difficult to examine the influence of temperatures on tensile strength at the same loading rates. Hence, the fitted tensile strength under five specific loading rates (100, 200, 300, 400, and 500 GPa/s, respectively) were obtained by the fitting functions in Fig. 7(a), as shown in Table 3. The relationships between the tensile strength and temperatures at the five loading rates were fitted, as shown in Fig. 8. It was found that tensile strength and temperatures also obeyed the quadratic function relationship, and all the correlation coefficients were greater than 0.8. The fitting functions of tensile strength with temperatures or loading rates are shown in Table 4. Eqs. (1)–(5) are the relationship

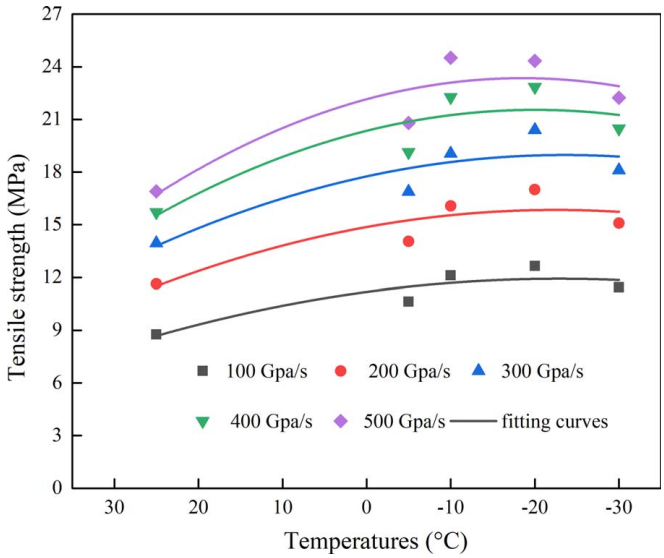

Fig. 8. Change relationships of dynamic tensile strength with temperatures.

Table 4. Regression equations of sandstone tensile strength with loading rate or temperature

Curves	Equation	R^2
1	$\sigma_t = -2.78 \times 10^{-5}\dot{\sigma}_t^2 + 0.037\dot{\sigma}_t + 5.35$ ($T = 25°C$)	0.989
2	$\sigma_t = -2.93 \times 10^{-5}\dot{\sigma}_t^2 + 0.043\dot{\sigma}_t + 6.625$ ($T = -5°C$)	0.992
3	$\sigma_t = -2.84 \times 10^{-5}\dot{\sigma}_t^2 + 0.048\dot{\sigma}_t + 7.607$ ($T = -10°C$)	0.993
4	$\sigma_t = -4.797 \times 10^{-5}\dot{\sigma}_t^2 + 0.058\dot{\sigma}_t + 7.325$ ($T = -20°C$)	0.994
5	$\sigma_t = -3.172 \times 10^{-5}\dot{\sigma}_t^2 + 0.046\dot{\sigma}_t + 7.159$ ($T = -30°C$)	0.993
6	$\sigma_t = -0.0014T^2 - 0.065T + 11.184$ ($\dot{\sigma}_t = 100$ GPa/s)	0.825
7	$\sigma_t = -0.0019T^2 - 0.087T + 14.868$ ($\dot{\sigma}_t = 200$ GPa/s)	0.803
8	$\sigma_t = -0.0022\ T^2 - 0.104T + 17.752$ ($\dot{\sigma}_t = 300$ GPa/s)	0.802
9	$\sigma_t = -0.003T^2 - 0.119T + 20.35$ ($\dot{\sigma}_t = 400$ GPa/s)	0.805
10	$\sigma_t = -0.0035T^2 - 0.13T + 22.149$ ($\dot{\sigma}_t = 500$ GPa/s)	0.818

functions of the curves in Fig. 7(a), and Eqs. (6)–(10) are the relationship functions of Fig. 8.

Table 4 shows the relationships between tensile strength σ_t and a single factor of loading rate $\dot{\sigma}_t$ or freezing temperature T, respectively. However, the dynamic loading test of sandstone was carried out under the effect of real-time freezing in this paper. Therefore, it was necessary to further establish the regression model of sandstone tensile strength under the effect of temperature and loading rate, in order to more accurately predict mechanical properties of slope rock in the process of loose blasting under the cold environment. According to the regression results of a single factor, a quadratic function regression model was established for the interaction of two factors. In particular, the cross term of temperature and loading rate was introduced, and finally, the prediction model of tensile strength was established, as shown in Eq. (3). The data analysis software SPSS 19.0 was used to modify and test the established prediction model based on the experimental data and the estimated parameters are shown in Table 5.

$$\sigma_t = aT + b\dot{\sigma}_t + cT^2 + d\dot{\sigma}_t^2 + eT\dot{\sigma}_t + f \tag{3}$$

where a, b, c, d, e, f = model parameters, and the remaining variables are consistent with those in Table 2.

It should be noted that the regression coefficients (a, b, c, d, and e) in the regression model were the results after standardization, so the influence degree of different independent variables on dependent variables can be directly compared through the absolute value of the regression coefficients. It can be seen from Table 5 that the influence of temperature on the tensile strength of water-saturated sandstone is greater than that of the loading rate. In addition, the standard error and 95% confidence interval in the regression analysis were used to evaluate the accuracy of parameter estimation (Farrokhrouz et al. 2014; Yilmaz 2010). The smaller the standard error value of the parameter estimated, the more accurate the parameter estimate is. As can be seen from Table 5, the standard error of the estimated values of each parameter is close to zero, indicating that the accuracy of the estimated results of each parameter can meet the requirements after the iterative operation. It should be noted that the estimated value of the parameter is zero, indicating that the cross term of temperature and loading rate in the model has no statistical significance. In particular, the influence of temperature and loading rate on the tensile strength can be ignored in the test process. Therefore, after the nonlinear regression correction, the prediction model obtained in this experiment is Eq. (1), shown in Table 6. In addition, a regression model [Eq. (2) in Table 6] of the tensile strength of Laurentian Granite with loading rate and high temperature based on the data in the literature (Yin et al. 2015) was also given. In this study, the reliability of the established model was verified by using its root-mean square error (RMSE) and variance (VAF) (Finol et al. 2001; Yilmaz and Yuksek 2008, 2009), and the calculation equations of RMSE and VAF are shown in the following equation:

$$\begin{cases} \mathrm{RMSE} = \sqrt{\dfrac{1}{N}\displaystyle\sum_{i=1}^{N}(y_i - y_i^*)^2} \\ \mathrm{VAF} = \left(1 - \dfrac{\mathrm{var}(y_i - y_i^*)}{\mathrm{var}(y_i)}\right) \times 100 \end{cases} \tag{4}$$

where N = number of samples; and y_i and y_i^* = measured values and predicted values, respectively. If the values of RMSE and VAF are close to 0 and 100, respectively, the prediction model will be very suitable. The values of VAF and RMSE in Table 6 indicated a better prediction performance of the model (3). Results of regression analyses showed very good correlations, and VAF and RMSE indices revealed higher prediction performance.

The 1:1 slope line graph can intuitively reflect the prediction accuracy of the model (Gokceoglu 2002; Yasar and Erdogan 2004). Fig. 9 shows the distribution of the data points determined by the predicted values and their corresponding measured values in the 1:1 slope line graph. It can be seen from Fig. 9 that the data points are more evenly distributed on both sides of the 1:1 slope line, and the distance from data points to the slope line, representing prediction error, is small. It indicates that the model can accurately predict the variation of rock tensile strength values with loading rate and temperature.

Table 5. Parameter estimates

			95% confidence interval	
Parameter	Estimate	Std. error	Lower bound	Upper bound
a	−0.056	0.013	−0.082	−0.030
b	0.047	0.005	0.038	0.056
c	−0.002	0.000	−0.003	−0.001
d	-4.055×10^{-5}	0.000	-5.724×10^{-5}	-2.386×10^{-5}
e	0.000	0.000	0.000	-4.552×10^{-5}
f	7.271	0.557	6.159	8.384

Failure Process and Characteristics

Dynamic Failure Process of Samples

The dynamic failure process of the sample was captured by a high-speed camera system (Phantom v611 high-speed camera) during the test, and the initiation and expansion process of the cracks at different times was obtained. Figs. 10 and 11 show the dynamic failure process of the sample under normal temperature (25°C) and −20°C, respectively.

In Figs. 10(b) and 11(b), cracks initiated from the center of samples under normal and freezing conditions, and this phenomenon has been obtained by many studies (Gomez et al. 2001; Wong et al. 2014; Yin et al. 2015). It indicates that this test meets the standards of the BD test. After the generation of the main cracks at the center of the samples, they expanded along the loading direction until they penetrated the samples. In addition, at the contact of the pressure bars with the samples, significant shear failure zones were due to stress concentration. It is worth noting that the generation and propagation of the main cracks in the two sets of samples were earlier than the secondary cracks extending from the contact ends. Therefore, the secondary cracks did not affect the dynamic tensile process (Zhang and Zhao 2013). The aforementioned

Table 6. Regression model and its R^2, RMSE, and VAF

Equation	R^2	RMSE	VAF
$\sigma_t = -0.056T + 0.047\dot{\sigma}_t - 0.002T^2 + 4.055 \times 10^{-5}\dot{\sigma}_t^2 + 7.271$	0.950	0.894	95.03
$\sigma_t = 0.001T + 0.024\dot{\sigma}_t - 1.709 \times 10^{-5}T^2 - 3.694 \times 10^{-6}\dot{\sigma}_t^2 - 5.04 \times 10^{-6}T\dot{\sigma}_t + 15.261$	0.976	1.643	97.55

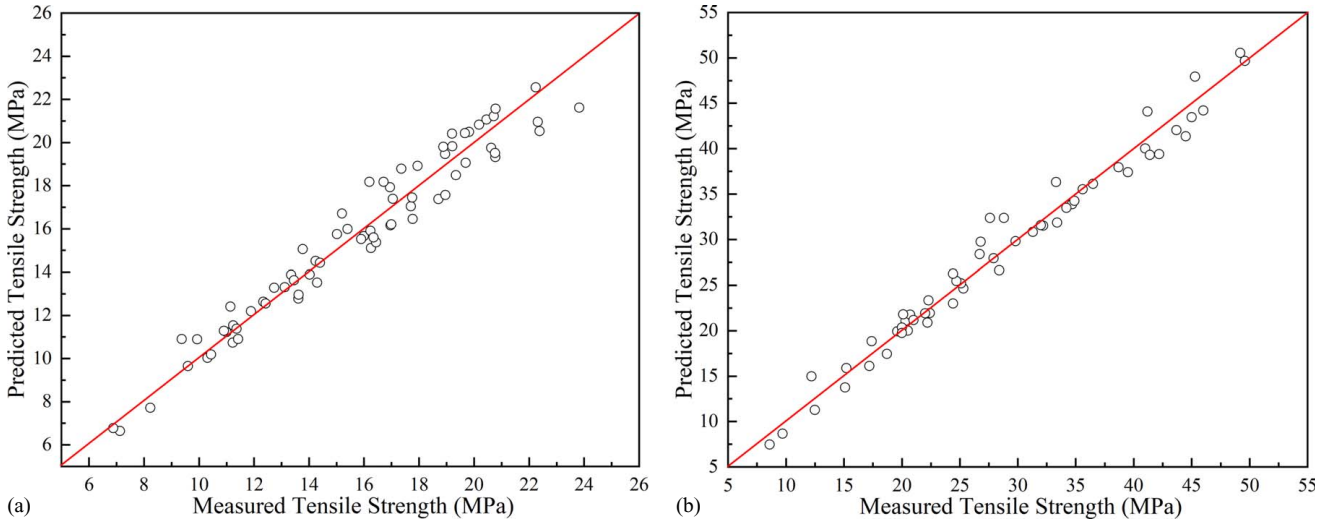

Fig. 9. Verify the accuracy of the prediction model: (a) dynamic tensile test of slope sandstone at different low temperature (this study); and (b) dynamic tensile test of Laurentian granite at different high temperature (data from Yin et al. 2015).

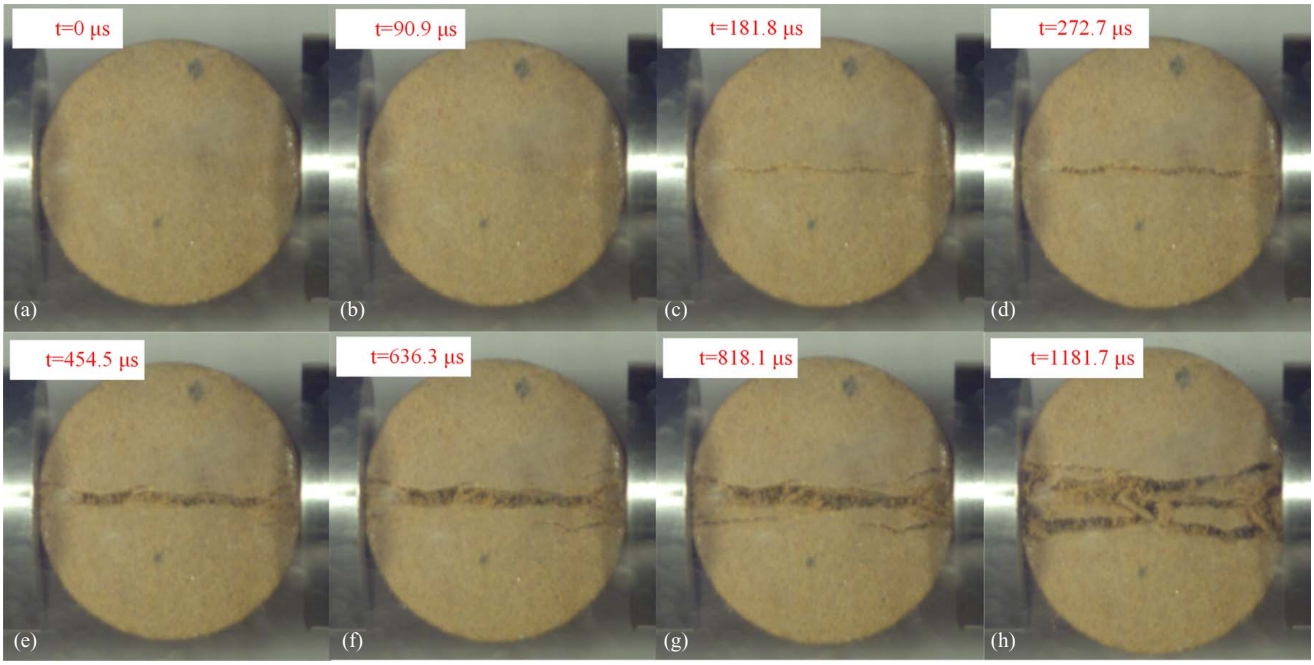

Fig. 10. Dynamic failure process of samples at normal temperature (25°C).

phenomena are common characteristics of dynamic tensile experiments.

The differences in the failure process of the samples under two temperature conditions are mainly manifested in two aspects. In the first aspect, a large number of secondary cracks can be observed at both ends of the sample under normal temperature (25°C) after the main cracks penetrated the sample from Figs. 10(e–h). The secondary cracks gradually merged with the main crack as the loading process proceeded and participated in the failure of the samples. However, the secondary cracks initiation and propagation during the failure process at −20°C were not obvious. This difference was mainly due to the water in cracks and pores of the original sample condensing into ice at low temperature, which enhanced the cohesion between the particles and compactness of the structure of the sample. The sample at normal temperature has a large number of large-volume bulks and small-volume powders in the fracture zone due to the expansion and connectivity of secondary cracks [Fig. 10(h)]. The integrity of the sample after failure was also different from that under freezing. The second aspect of the failure process of the samples under two typical conditions was the roughness of the fracture surface. It can be seen that the fracture surface formed during the failure process of the frozen sample was flatter than that at normal temperature by comparing Fig. 10 with Fig. 11. This is the result of the enhanced brittleness of sandstone under low temperatures, and the failure showed obvious characteristics of the brittle fracture.

Characteristics of Samples after Failure

Fig. 12 shows the failure patterns of sandstone samples at different freezing temperatures. It can be seen that the failure areas of the sample at normal temperature were significantly larger than that

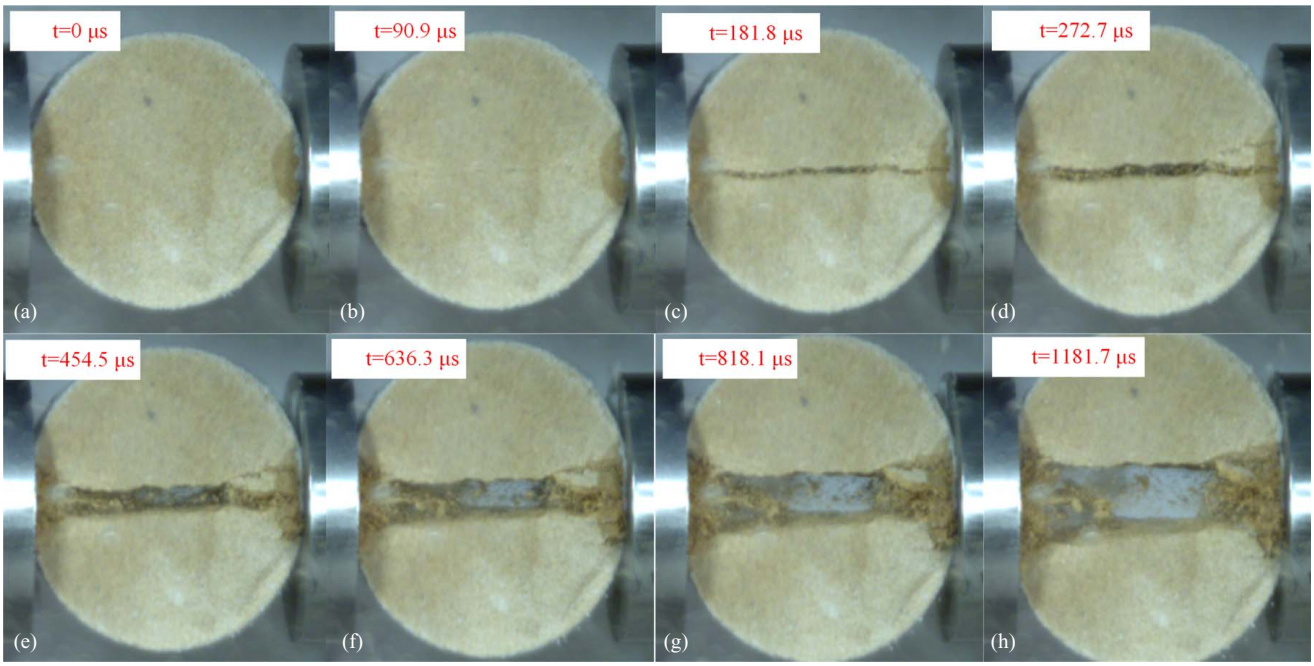

Fig. 11. Dynamic failure process of the sample at −20°C.

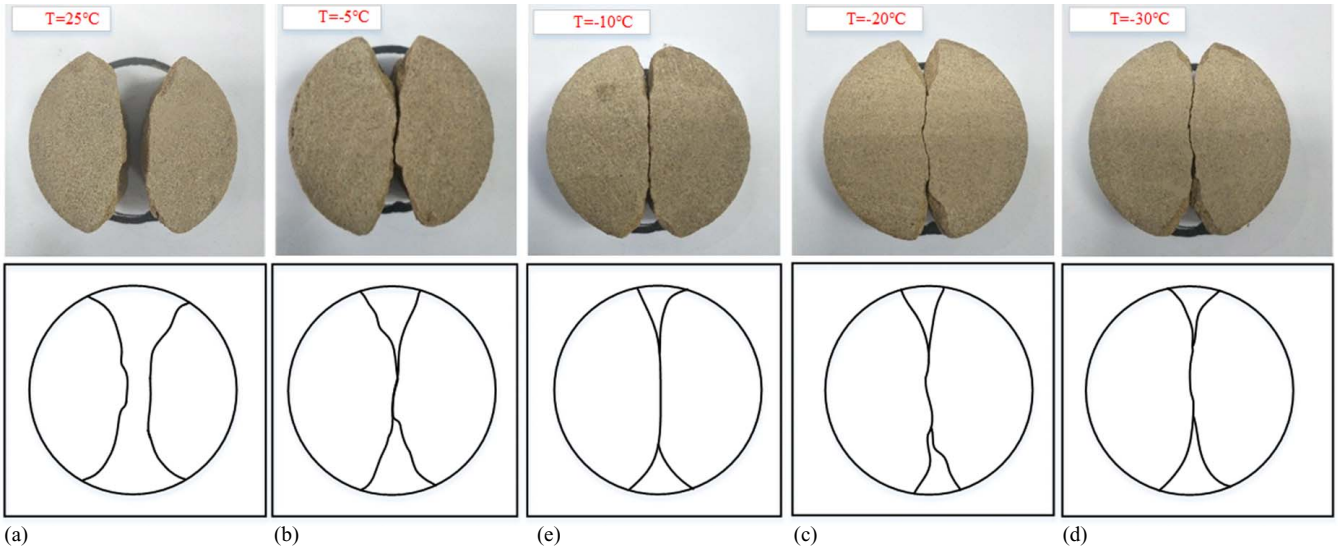

Fig. 12. Failure morphology of sandstone samples at different temperatures.

of other groups under freezing conditions. A damaged loss zone appears in the middle of the sample at normal temperature. Whereas the frozen groups of samples all just formed triangular shear failure zones at both ends of the load. The failure patterns of the freezing samples were shown as the tear in the middle along the loading line, and the range of the shear failure zone at both ends did not extend to the center of the samples. Failure patterns of the frozen samples from four groups were approximately the same. The triangular shear failure zone of the sample with the freezing temperature at −5°C was significantly larger than that of the other three groups of frozen samples, and failure zones of the three groups at −10°C, −20°C, and −30°C were similar in size. The size of the damage zone of the five groups of samples was related to tensile strength at different temperature conditions with the same loading rate.

Fracture Characteristics of Fracture Surface

Macrofracture Characteristics of Samples at Different Temperatures

Roughness is one of the most important characterization parameters of macroscopic fracture characteristics, and it is formed by the initiation and propagation of cracks under the action of external forces. The quantitative analysis of roughness can better study the effect of low temperature on rock fracture.

Test Method and Test Equipment of Fracture Roughness

In a previous study (Huang et al. 2018; ISRM 1981; Rong et al. 2016), scholars were inclined to use the method proposed by Tse and Cruden (1979) to characterize the roughness of a

three-dimensional fracture surface. This method is to divide the fracture surface into several equidistant lines along the length direction to extract several two-dimensional profiles and then calculate some linear parameters of these two-dimensional profiles to characterize the joint roughness coefficient (JRC) value of the three-dimensional fracture surface. However, the essence of this method is the two-dimensional simulation of roughness. In order to understand the geometry of the three-dimensional fracture surface more accurately, the three-dimensional features need to be quantified (Magsipoc et al. 2020; Tatone and Grasselli 2012). In recent years, it has become possible to characterize roughness in three-dimensional methods with the development of laser scanners (Tatone and Grasselli 2009, 2013).

This test used a high-resolution noncontact JR three-dimensional scanning system to scan the effective tensile area with a size of 40 × 20 mm located in the center of the fracture surface of samples, as shown in Fig. 13. This system, which was developed by the State Key Laboratory of Geomechanics and Deep Underground Engineering, adopted the raster photography technology to acquire three-dimensional data of the fracture surface in a short time. The scanned data, which were automatically recorded in 0.1 mm increments along the fracture plane and had a vertical precision of ±1 μm, were then used to digitalize the rock fracture surfaces. In addition, three-dimensional roughness parameters

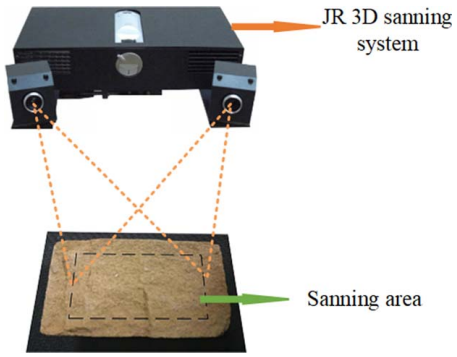

Fig. 13. JR 3D scanning system and scanning area of the fracture surface. (Images by Gang Lin.)

(asperity height, slope angle, and aspect) were selected to characterize the roughness of the fracture surface in this study (Sharifzadeh et al. 2008). This method divided the fracture surface into several grid regions with a size of 0.1 × 0.1 mm, as shown in Fig. 14. The asperity height of a grid region denotes the height from the average surface height, the slope angle denotes the angle between normal vectors on each grid region from the *Z*-direction, and the aspect denotes the projection of the grid region orientation with respect to the *X*-direction. Roughness is a collection characterized by the statistical values of asperity height, slope angle, and aspect on the surface of several grid regions (Yin et al. 2017, 2019).

Variation of Roughness with Freezing Temperature

After dividing the fracture surface into several grid regions, the statistics of the asperity height, slope angle, and aspect on each grid area were counted. The statistical data included the maximum, minimum, mean, and standard deviation of asperity height, slope angle, and aspect, as shown in Fig. 15. Among them, the standard deviation is the degree of dispersion of the values relative to the mean value on the fracture surface, and it can best reflect the variation of roughness, waviness, and undulation of the fracture surface. It could be seen that the standard deviations (stDev) of the asperity heights are 0.87737 and 0.46821 mm from Figs. 15(a and d) when $T = 25$ and −20°C, respectively. The stDev of the slope angle are 11.4938° and 7.7122°, respectively. Figs. 15(a and d) also shows a polar plot of the aspect direction–frequency distribution, with standard deviations of 104.344° and 100.763°, respectively. It can be seen that the standard deviations of the asperity height, slope angle, and aspect at −20°C were smaller than those at normal temperature. Namely, the roughness of the fracture surface of the sample at −20°C was significantly lower than that at normal temperature.

Fig. 16 shows the variation of the standard deviation of asperity height, slope angle, and aspect on the fracture surface with different temperatures, and it can be seen that their trends are approximately the same. The overall change process can be divided into the normal temperature stage and freezing stage. The asperity height, slope angle, and aspect of the fracture surfaces at normal temperature (25°C) are 39.7%, 35.1%, and 1.7% higher than those at −5°C, respectively. It can be seen that the low temperature has an important

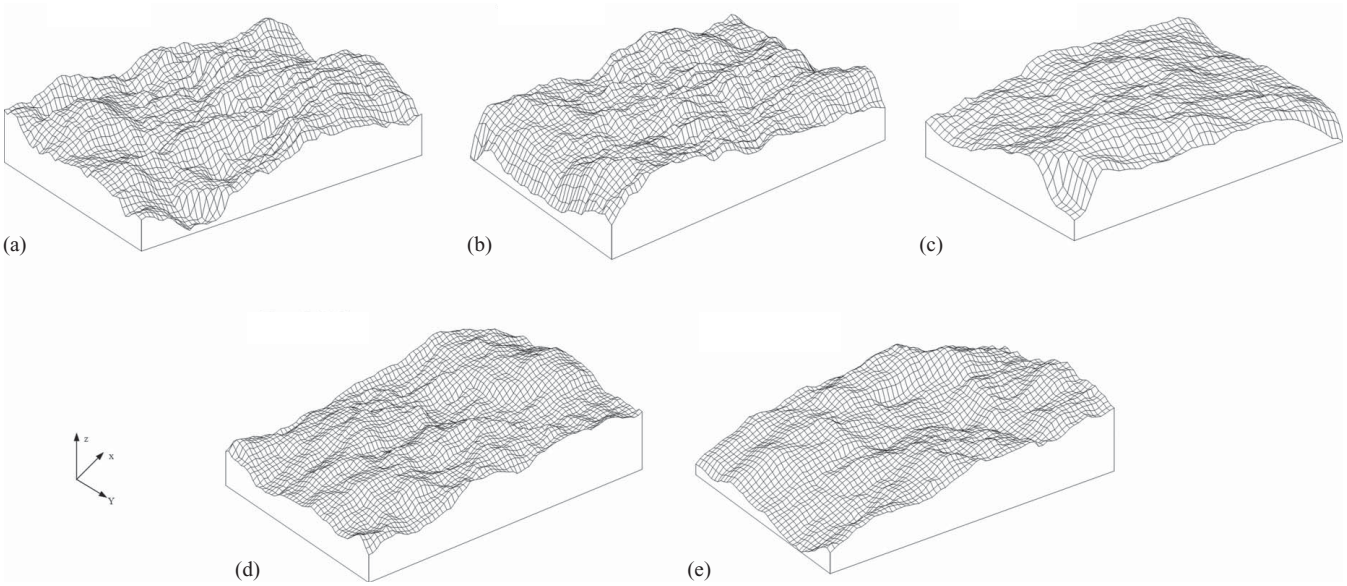

Fig. 14. Surface topographies of rock fractures at different temperatures: (a) $T = 25$°C; (b) $T = -5$°C; (c) $T = -10$°C; (d) $T = -20$°C; and (e) $T = -30$°C.

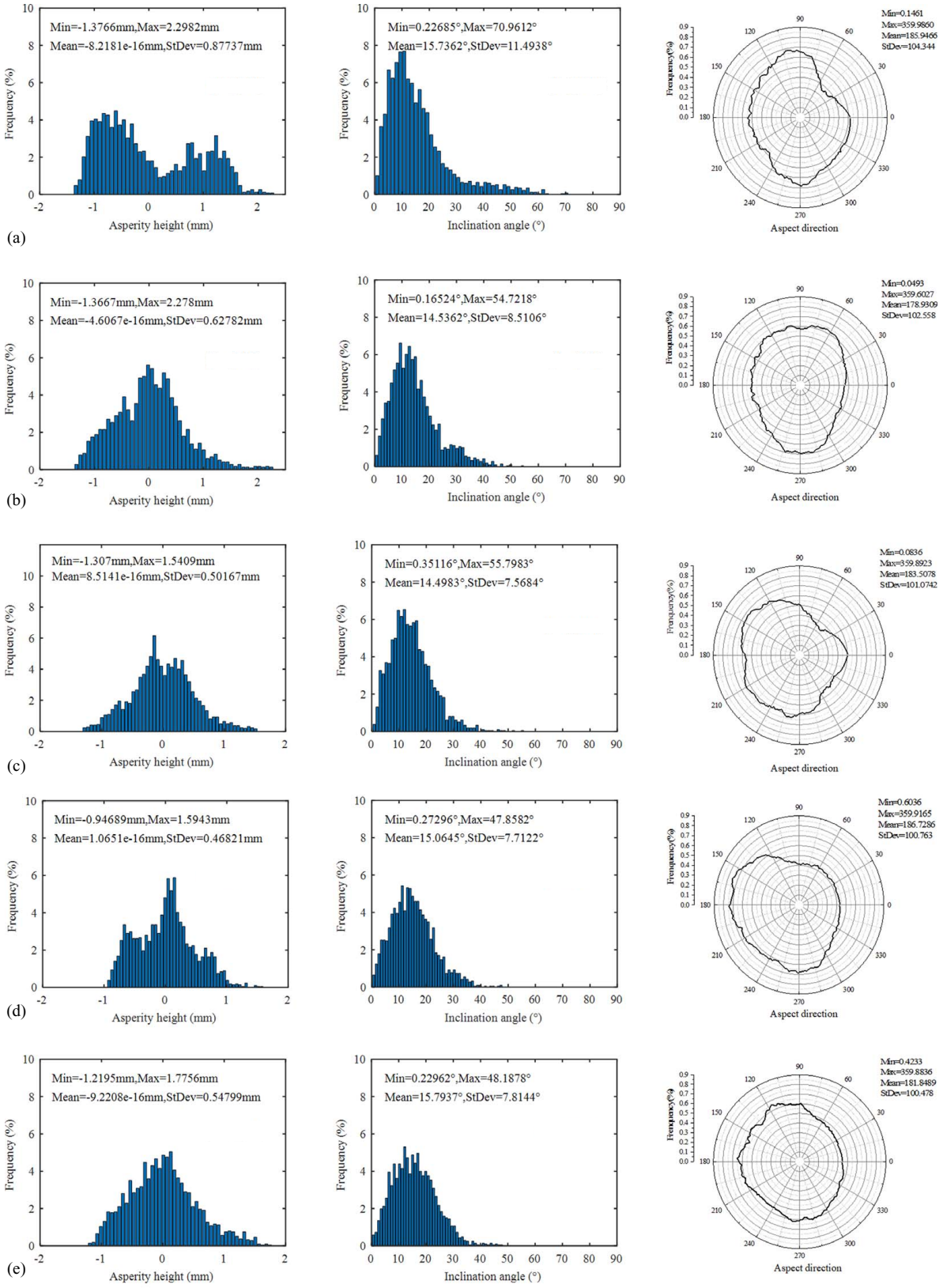

Fig. 15. Asperity height, slope angle, aspect direction–frequency distributions of the tested fracture surfaces: (a) normal temperature (25°C); (b) −5°C; (c) −10°C; (d) −20°C; and (e) −30°C.

influence on the roughness of the dynamic tensile failure of rocks. In addition, the roughness of the fracture surfaces at four different freezing temperatures is also different. The fracture roughness at −5°C is greater than that of the other three groups at low temperature, and the reasons will be explained in ++Section 5.2 by the changes in the microscopic morphological characteristics of the fracture surface. Whereas no obvious variation laws of roughness were found in the three groups of −10°C, −20°C, and −30°C.

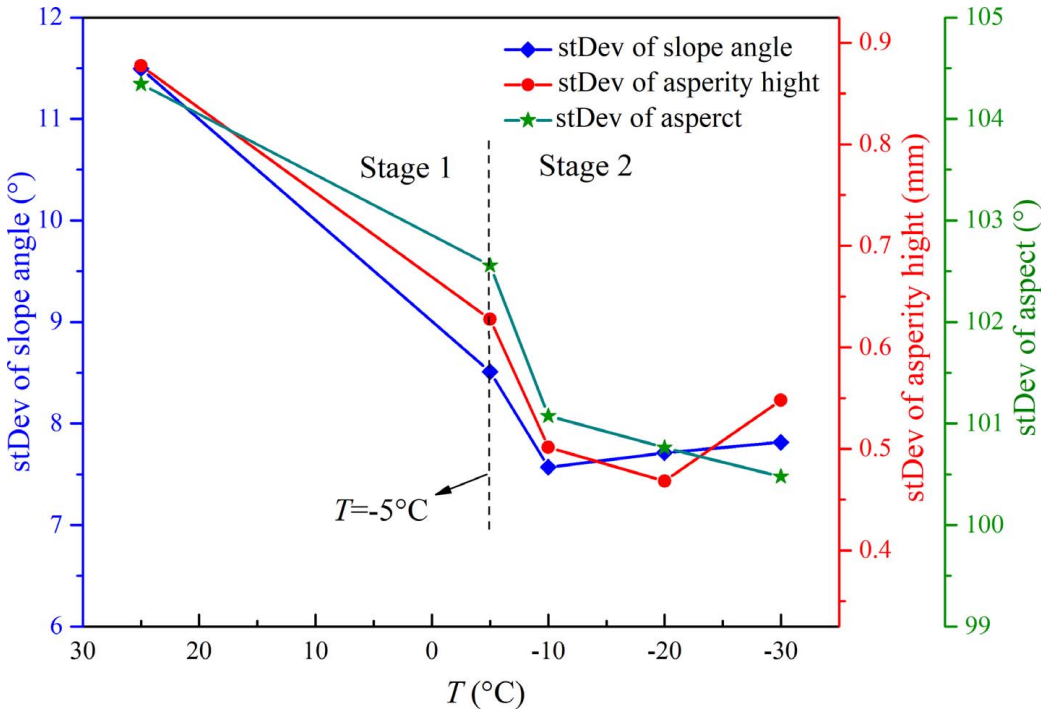

Fig. 16. Variation laws of the standard deviation of asperity height, slope angle, and aspect direction with different temperatures.

Mesofracture Characteristics of Samples at Different Temperatures

In order to further understand the fracture mechanism of sandstone samples at different temperatures, the fracture surface of sandstone samples was scanned by scanning electron microscopy (SEM), and the mesoscopic morphological characteristics of dynamic tensile fracture of sandstone were determined under different temperatures.

Test Equipment and Test Process

The TESCAN VEGA3 SEM test system was adopted in this test to scan the mesoscopic morphological characteristics of the fracture surface. The specific test process is as follows. First, a round sheet was made with a diameter of 10 mm and a thickness of about 2 mm from the fracture surface to be observed and dried in a constant-temperature drying box for 12 h. Second, a fine brush was used to remove the debris from the surface, and the samples were gilded before the test began. Finally, the prepared sample to be observed was fixed to an observation platform, and an electron microscope scanning test was performed.

Variation of Mesoscopic Morphologies Characteristics with Freezing Temperature

The macrofracture characteristics of rocks were determined by the changes of mesofracture characteristics (Zhou et al. 2020). The mesofracture characteristics are the traces left on the fracture surface during the fracture process. Through the analysis of these traces, the mechanism of macroscopic fracture characteristics can be clarified. Different fracture modes correspond to different mesoscopic morphologies. The mesoscopic morphologies of the brittle fracture model mainly include river patterns, lamellar tearing patterns, step patterns, candy patterns, and intergranular cracks. The mesoscopic morphologies of the ductile fracture model mainly include dimple patterns, slip-separation patterns, striped patterns, and transgranular cracks (Derdk 1999; Li et al. 2019; Xie and Chen 1989; Xu et al. 2009; Zhang et al. 2020; Zuo et al. 2007).

Fig. 17 shows the fracture surfaces of the samples amplified by 100, 500, and 1,000 times after the impact of dynamic load. Through observing the fracture surfaces at different magnifications, it can be seen that it is difficult to extract effective fracture morphological information at low magnifications (100 times). Only the roughness of the fracture surfaces can be roughly observed, the mesoscopic morphological information on the fracture surface needed to be further magnified and observed. From Fig. 17(a), a slip-separation pattern can be observed on the fracture surface at normal temperature under 500 times magnification. After being further magnified to 1,000 times, in addition to the sliding separation patterns, there are also clustered dimples. Slip-separation and dimples were both typical ductile morphologies, which were formed by plastic deformation caused by friction between particles and cement during the fracture process. Therefore, the fracture mode of the sample was a ductile fracture. From Fig. 17(b), river patterns and step patterns were observed on the fracture surface of the sample under −5°C and the dimple patterns were also found under high magnification observation conditions. However, the dimple was a single, isolated morphology and did not form dimple clusters. The main fracture mode under this temperature was a brittle fracture, which locally showed a ductile fracture. From Figs. 17(c–e), it can be seen that on the fracture surface at freezing temperatures of −10°C, −20°C, and −30°C, the mesofracture morphologies include river patterns, lamellar tearing patterns, step patterns, and intergranular crystals, belonging to typical brittle fracture morphologies. The fracture modes were all marked brittle fractures. The low temperature makes the fracture model of the saturated sample change from ductile fracture under normal temperature to brittle fracture. Compared with brittle fracture mode, the ductile fracture will cause more plastic deformation on the fracture surface, which is the reason why the macroscopic fracture roughness of frozen samples is

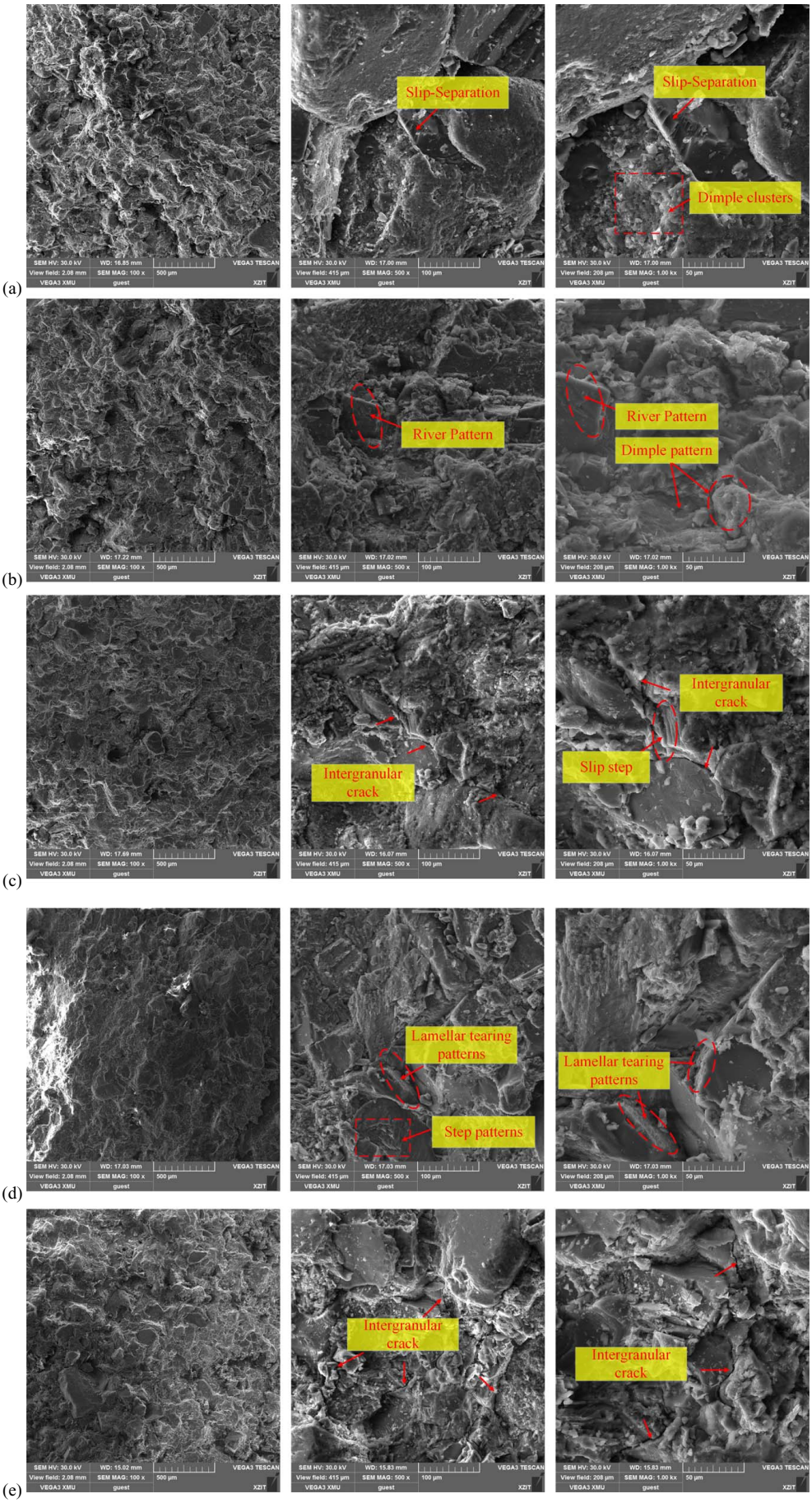

Fig. 17. Mesoscopic morphologies of fracture surfaces: (a) normal temperature (25°C); (b) −5°C; (c) −10°C; (d) −20°C; and (e) −30°C.

smaller than that at normal temperature after dynamic tensile failure.

Conclusions

In this paper, the SHPB test system was used to study the dynamic splitting tensile strength of the slope sandstone in Beitashan Pasture Coal Mine under different temperatures (25°C, −5°C, −10°C, −20°C, and −30°C). The dynamic failure process, the roughness of the fracture surfaces after the failure, and the mesomorphological characteristics after the failure were observed and analyzed. The following conclusions can be drawn:

1. The dynamic tensile strength of sandstone samples at different temperatures increased with the increase of the loading rate. At the same loading rate, the dynamic tensile strength first increased with decreasing freezing temperature and then decreased, and −20°C was the inflection point temperature of strength change.
2. Based on the experimental data, a prediction model for the strength change of sandstone under the combined effect of temperature and loading rate was established [Eq. (3)]. The model was revised and tested by nonlinear regression analysis, and the results showed that the proposed model could accurately and reliably predict the change law of the tensile strength under the impacts of temperature and loading rate.
3. The cracks of the samples at normal temperature and freezing temperatures all initiated from the center of the samples until the cracks penetrated the samples. In the case of sample failure at normal temperature, a large number of secondary cracks appeared near the loading ends, and then the secondary cracks and the main cracks merged with each other, resulting in complex failure of the sample at normal temperature. The damaged loss zone was formed in the center of the sample after the failure. This phenomenon did not occur in the failure process at freezing temperature, and only shear failure zones were formed at the loading ends after the failure.
4. The standard deviations of the roughness parameters (asperity height, slope angle, and aspect) of the fracture surface at normal temperature were significantly greater than those at freezing temperature. However, no obvious laws were found for the change of fracture roughness at different freezing temperatures. Observations showed that the ductile mesofracture morphologies of the fracture surface were remarkable at normal temperature. With the introduction of a low-temperature gradient, the fracture mode of the samples was transformed into a significant brittle fracture. The change of mesofracture characteristics was the root cause of the change in the macroroughness of the fracture surface.

In this paper, only the slope sandstone samples were selected as the research objects, and the dynamic strength change laws of different types of rocks at low temperatures need to be further explored by experiments. In addition, the comparison of the dynamic and static mechanical properties of rocks at low temperature and their mechanism of changes will be carried out in the follow-up research.

Data Availability Statement

All data, models, and codes generated or used during the study appear in the published article.

Acknowledgments

Financial support for this work was provided by the National Natural Science Foundation (Grant Nos. Z4U179534, Z4U194686, 51704281 and 12072363).

References

Ai, D. H., Y. C. Zhao, Q. F. Wang, and C. W. Li. 2020. "Crack propagation and dynamic properties of coal under SHPB impact loading: Experimental investigation and numerical simulation." *Theor. Appl. Fract. Mech.* 105: 102393. https://doi.org/10.1016/j.tafmec.2019.102393.

Aoki, K., K. Hibiya, and T. Yoshida. 1990. "Storage of refrigerated liquefied gases in rock caverns: Characteristics of rock under very low temperatures." *Tunnelling Underground Space Technol.* 5 (4): 319–325. https://doi.org/10.1016/0886-7798(90)90126-5.

Azimian, A., and R. Ajalloeian. 2015. "Empirical correlation of physical and mechanical properties of marly rocks with P wave velocity." *J. Geosci.* 8 (4): 2069–2079. https://doi.org/10.1007/s12517-013-1235-4.

Chen, L., X. B. Mao, S. L. Yang, C. An, and P. Wu. 2019. "Experimental investigation on dynamic fracture mechanism and energy evolution of saturated yellow sandstone under different freeze-thaw temperatures." *Adv. Civ. Eng.* 2019: 2375276. https://doi.org/10.1155/2019/2375276.

Chen, T. C., M. R. Yeung, and N. Mori. 2004. "Effect of water saturation on deterioration of welded tuff due to freeze-thaw action." *Cold Reg. Sci. Technol.* 38 (2–3): 0–136. https://doi.org/10.1016/j.coldregions.2003.10.001.

Chen, W., B. Song, D. J. Frew, and M. J. Forrestal. 2003. "Dynamic small strain measurements of a metal specimen with a split Hopkinson pressure bar." *Exp. Mech.* 43 (1): 20–23. https://doi.org/10.1007/BF02410479.

Dai, F., R. Chen, and K. Xia. 2010a. "A semi-circular bend technique for determining dynamic fracture toughness." *Exp. Mech.* 50 (6): 783–791. https://doi.org/10.1007/s11340-009-9273-2.

Dai, F., S. Huang, K. W. Xia, and Z. Y. Tan. 2010b. "Some fundamental issues in dynamic compression and tension tests of rocks using split Hopkinson pressure bar." *Rock Mech. Rock Eng.* 43 (6): 657–666. https://doi.org/10.1007/s00603-010-0091-8.

Derdk, H. 1999. *Fractography*. Cambridge, UK: Cambridge University Press.

Dwivedi, R. D., A. K. Soni, R. K. Goel, and A. K. Dube. 2000. "Fracture toughness of rocks under sub-zero temperature conditions." *Int. J. Rock Mech. Min. Sci.* 37 (8): 1267–1275. https://doi.org/10.1016/S1365-1609(00)00051-4.

Farrokhrouz, M., M. R. Asef, and R. Kharrat. 2014. "Empirical estimation of uniaxial compressive strength of shale formations." *Geophysics* 79 (4): D227–D233. https://doi.org/10.1190/geo2013-0315.1.

Finol, J., Y. K. Guo, and X. D. Jing. 2001. "A rule based fuzzy model for the prediction of petrophysical rock parameters." *J. Pet. Sci. Eng.* 29 (2): 97–113. https://doi.org/10.1016/S0920-4105(00)00096-6.

Gokceoglu, C. 2002. "A fuzzy triangular chart to predict the uniaxial compressive strength of the Ankara agglomerates from their petrographic composition." *Eng. Geol.* 66 (1–2): 39–51. https://doi.org/10.1016/S0013-7952(02)00023-6.

Gomez, J. T., A. Shukla, and A. Sharma. 2001. "Static and dynamic behavior of concrete and granite in tension with damage." *Theor. Appl. Fract. Mech.* 36 (1): 37–49. https://doi.org/10.1016/S0167-8442(01)00054-4.

Gong, F. Q., and J. Hu. 2020. "Energy dissipation characteristic of red sandstone in the dynamic Brazilian disc test with SHPB setup." *Adv. Civ. Eng.* 2020: 7160937. https://doi.org/10.1155/2020/7160937.

Huang, N., R. C. Liu, Y. Y. Jiang, B. Li, and L. Y. Yu. 2018. "Effects of fracture surface roughness and shear displacement on geometrical and hydraulic properties of three-dimensional crossed rock fracture models." *Adv. Water Resour.* 113: 30–41. https://doi.org/10.1016/j.advwatres.2018.01.005.

Hughes, M. L., J. W. Tedesco, and C. A. Ross. 1993. "Numerical analysis of high strain rate splittingtensile tests." *Comput. Struct.* 47 (4–5): 653–671. https://doi.org/10.1016/0045-7949(93)90349-I.

Inada, Y., and K. Yokota. 1984. "Some studies of low temperature rock strength." *Int. J. Rock Mech. Min. Sci. Geomech. Abstr.* 21 (3): 145–153. https://doi.org/10.1016/0148-9062(84)91532-8.

ISRM (International Society for Rock Mechanics). 1978. "Suggested methods for determining tensile strength of rock materials." *Int. J. Rock Mech. Min. Sci. Geomech. Abstr.* 15 (3): 99–103. https://doi.org/10.1016/0148-9062(78)90003-7.

ISRM. 1981. "Rock characterization, testing and monitoring-ISRM suggested methods." In *Suggested methods for the quantitative description of discontinuities in rock masses*, edited by E. T. Brown, 3–52. Oxford: Pergamon.

Karakul, H., and R. Ulusay. 2013. "Empirical correlations for predicting strength properties of rocks from P-wave velocity under different degrees of saturation." *Rock Mech. Rock Eng.* 46 (5): 981–999. https://doi.org/10.1007/s00603-012-0353-8.

Kolsky, H. 1949. "An investigation of the mechanical properties of materials at very high rates of loading." *Proc. Phys. Soc. B* 62 (11): 676–700. https://doi.org/10.1088/0370-1301/62/11/302.

Kolsky, H. 1953. Vol. 3 of *Stress waves in solids*, 83–84. Oxford, UK: Clarendon Press.

Korshunov, A. A., S. P. Doroshenko, and A. L. Nevzorov. 2016. "The impact of freezing–thawing process on slope stability of earth structure in cold climate." *Procedia Eng.* 143: 682–688. https://doi.org/10.1016/j.proeng.2016.06.100.

Lai, Y. M., S. M. Zhang, and W. B. Yu. 2012. "A new structure to control frost boiling and frost heave of embankments in cold regions." *Cold Reg. Sci. Technol.* 79–80: 53–66. https://doi.org/10.1016/j.coldregions.2012.04.002.

Li, J. L., R. B. Kaunda, and K. P. Zhou. 2018a. "Experimental investigations on the effects of ambient freeze–thaw cycling on dynamic properties and rock pore structure deterioration of sandstone." *Cold Reg. Sci. Technol.* 154: 133–141. https://doi.org/10.1016/j.coldregions.2018.06.015.

Li, J. L., K. P. Zhou, W. J. Liu, and Y. M. Zhang. 2018b. "Analysis of the effect of freeze–thaw cycles on the degradation of mechanical parameters and slope stability." *Bull. Eng. Geol. Environ.* 77 (2): 573–580. https://doi.org/10.1007/s10064-017-1013-8.

Li, M., G. Lin, W. Zhou, X. B. Mao, L. Y. Zhang, and R. R. Mao. 2019. "Experimental study on dynamic tensile failure of sandstone specimens with different water contents." *Shock Vib.* 2019: 7012752. https://doi.org/10.1155/2019/7012752.

Li, M., X. B. Mao, L. L. Cao, H. Pu, and A. H. Lu. 2017. "Influence of heating rate on the dynamic mechanical performance of coal measure rocks." *Int. J. Geomech.* 17 (8): 04017020. https://doi.org/10.1061/(ASCE)GM.1943-5622.0000888.

Liu, B., Y.-T. Gao, A.-B. Jin, and D. Elmo. 2020. "Fracture characteristics of orebody rock with varied grade under dynamic Brazilian tests." *Rock Mech. Rock Eng.* 53 (5): 2381–2398. https://doi.org/10.1007/s00603-020-02048-9.

Liu, B., N. Liu, D. Y. Li, G. Zhang, H. L. Deng, J. Wang, and S. J. Tang. 2017. "Frozen strength test on deep water-rich sandstone in Ordos." [In Chinese.] *J. Min. Sci. Technol.* 2017 (1): 29–36. https://doi.org/CNKI:SUN:KYKX.0.2017-01-005.

Liu, C. J., H. W. Deng, H. T. Zhao, and J. Zhang. 2018. "Effects of freeze–thaw treatment on the dynamic tensile strength of granite using the Brazilian test." *Cold Reg. Sci. Technol.* 155: 327–332. https://doi.org/10.1016/j.coldregions.2018.08.022.

Luo, X. D., N. Jiang, X. Y. Fan, N. F. Mei, and H. Luo. 2015. "Effects of freeze–thaw on the determination and application of parameters of slope rock mass in cold regions." *Cold Reg. Sci. Technol.* 110: 32–37. https://doi.org/10.1016/j.coldregions.2014.11.002.

Magsipoc, E., Q. Zhao, and G. Grasselli. 2020. "2D and 3D roughness characterization." *Rock Mech. Rock Eng.* 53 (3): 1495–1519. https://doi.org/10.1007/s00603-019-01977-4.

Park, C., J. H. Synn, H. S. Shin, D. S. Cheon, H. D. Lim, and S. W. Jeon. 2004. "An experimental study on the thermal characteristics of rock at low temperatures." *Int. J. Rock Mech. Min. Sci.* 41 (3): 367–368. https://doi.org/10.1016/j.ijrmms.2003.12.084.

Pei, P. D., F. Dai, Y. Liu, and M. D. Wei. 2020. "Dynamic tensile behavior of rocks under static pre-tension using the flattened Brazilian disc method." *Int. J. Rock Mech. Min. Sci.* 126: 104208. https://doi.org/10.1016/j.ijrmms.2019.104208.

Ping, Q., Q. Y. Ma, and P. Yuan. 2013. "Energy dissipation analysis of stone specimens in SHPB tensile test." [In Chinese.] *J. Min. Saf. Eng.* 30 (3): 401–407.

Renliang, S., S. Yongwei, S. Liwei, and B. Yao. 2019. "Dynamic property tests of frozen red sandstone using a split Hopkinson pressure bar." *Earthquake Eng. Eng. Vibr.* 18 (3): 511–519. https://doi.org/10.1007/s11803-019-0518-5.

Rong, G., J. Yang, L. Cheng, and C. Zhou. 2016. "Laboratory investigation of nonlinear flow characteristics in rough fractures during shear process." *J. Hydrol.* 541: 1385–1394. https://doi.org/10.1016/j.jhydrol.2016.08.043.

Sharifzadeh, M., Y. Mitani, and T. Esaki. 2008. "Rock joint surfaces measurement and analysis of aperture distribution under different normal and shear loading using GIS." *Rock Mech. Rock Eng.* 41 (2): 299–323. https://doi.org/10.1007/s00603-006-0115-6.

Tatone, B. S. A., and G. Grasselli. 2009. "A method to evaluate the three-dimensional roughness of fracture surfaces in brittle geomaterials." *Rev. Sci. Instrum.* 80: 125110. https://doi.org/10.1063/1.3266964.

Tatone, B. S. A., and G. Grasselli. 2012. "Quantitative measurements of fracture aperture and directional roughness from rock cores." *Rock Mech. Rock Eng.* 45 (4): 619–629. https://doi.org/10.1007/s00603-011-0219-5.

Tatone, B. S. A., and G. Grasselli. 2013. "An investigation of discontinuity roughness scale dependency using high-resolution surface measurements." *Rock Mech. Rock Eng.* 46 (4): 657–681. https://doi.org/10.1007/s00603-012-0294-2.

Tse, R., and D. M. Cruden. 1979. "Estimating joint roughness coefficients." *Int. J. Rock Mech. Min. Sci. Geomech. Abstr.* 16 (5): 303–307. https://doi.org/10.1016/0148-9062(79)90241-9.

Ulrich, T. J., and T. W. Darling. 2001. "Observation of anomalous elastic behavior in rock at low temperatures." *Geophys. Res. Lett.* 28 (11): 2293–2296. https://doi.org/10.1029/2000GL012480.

Wang, P., J. Y. Xu, X. Y. Fang, and P. X. Wang. 2017. "Energy dissipation and damage evolution analyses for the dynamic compression failure process of red-sandstone after freeze–thaw cycles." *Eng. Geol.* 221: 104–113. https://doi.org/10.1016/j.enggeo.2017.02.025.

Wang, P., J. Y. Xu, S. Liu, S. H. Liu, and H. Y. Wang. 2016. "A prediction model for the dynamic mechanical degradation of sedimentary rock after a long-term freeze–thaw weathering: Considering the strain-rate effect." *Cold Reg. Sci. Technol.* 131: 16–23. https://doi.org/10.1016/j.coldregions.2016.08.003.

Wang, Q., B. B. Wu, and Y. S. H. Guo. 2019. "Dynamic tensile failure of Laurentian granite subjected to triaxial confinement." *Geotech. Lett.* 9 (2): 116–120. https://doi.org/10.1680/jgele.18.00244.

Weng, L., Z. J. Wu, Q. S. Liu, and Z. Y. Wang. 2019. "Energy dissipation and dynamic fragmentation of dry and water-saturated siltstones under sub-zero temperatures." *Eng. Fract. Mech.* 220: 106659. https://doi.org/10.1016/j.engfracmech.2019.106659.

Wong, L. N. Y., C. J. Zou, and Y. Cheng. 2014. "Fracturing and failure behavior of carrara marble in quasistatic and dynamic Brazilian disc tests." *Rock Mech. Rock Eng.* 47 (4): 1117–1133. https://doi.org/10.1007/s00603-013-0465-9.

Wu, B. B., W. Yao, and K. W. Xia. 2015. "Dynamic tensile failure of rocks under static pre-tension." *Int. J. Rock Mech. Min. Sci.* 80: 12–18. https://doi.org/10.1016/j.ijrmms.2015.09.003.

Wu, B. B., W. Yao, and K. W. Xia. 2016. "An experimental study of dynamic tensile failure of rocks subjected to hydrostatic confinement." *Rock Mech. Rock Eng.* 49: 3855–3864. https://doi.org/10.1007/s00603-016-0946-8.

Xia, K. W., and W. Yao. 2015. "Dynamic rock tests using split Hopkinson (Kolsky) bar system – A review." *J. Rock Mech. Geotech. Eng.* 7 (1): 27–59. https://doi.org/10.1016/j.jrmge.2014.07.008.

Xie, H. P., and Z. D. Chen. 1989. "Analysis of rock fracture micromechanism." [In Chinese.] *J. China Coal Soc.* 2: 57–67.

Xing, H. Z., G. Wu, S. Dehkhoda, P. G. Ranjith, and Q. B. Zhang. 2019. "Fracture and mechanical characteristics of CO_2-saturated sandstone at extreme loading conditions." *Int. J. Rock Mech. Min. Sci.* 117: 132–141. https://doi.org/10.1016/j.ijrmms.2019.03.025.

Xu, X.-L., Z.-X. Kang, M. Ji, W.-X. Ge, and J. Chen. 2009. "Research of microcosmic mechanism of brittle-plastic transition for granite under high temperature." *Procedia Earth Planet. Sci.* 1 (1): 432–437. https://doi.org/10.1016/j.proeps.2009.09.069.

Yamabe, T., and K. M. Neaupane. 2001. "Determination of some thermo-mechanical properties of Sirahama sandstone under subzero temperature condition." *Int. J. Rock Mech. Min. Sci.* 38 (7): 1029–1034. https://doi.org/10.1016/S1365-1609(01)00067-3.

Yang, R. S., S. Fang, W. Li, Y. Yang, Z. J. G. Yue, and G. Engineering. 2019. "Experimental study on the dynamic properties of three types of rock at negative temperature." *Geotech. Geol. Eng.* 37: 455–464, https://doi.org/10.1007/s10706-018-0622-8.

Yasar, E., and Y. Erdogan. 2004. "Correlating sound velocity with the density, compressive strength and Young's modulus of carbonate rocks." *Int. J. Rock Mech. Min. Sci.* 41 (5): 871–875. https://doi.org/10.1016/j.ijrmms.2004.01.012.

Yilmaz, I. 2010. "Influence of water content on the strength and deformability of gypsum." *Int. J. Rock Mech. Min. Sci.* 47 (2): 342–347. https://doi.org/10.1016/j.ijrmms.2009.09.002.

Yilmaz, I., and A. G. Yuksek. 2008. "An example of artificial neural network (ANN) application for indirect estimation of rock parameters." *Rock Mech. Rock Eng.* 41 (5): 781–795. https://doi.org/10.1007/s00603-007-0138-7.

Yilmaz, I., and G. Yuksek. 2009. "Prediction of the strength and elasticity modulus of gypsum using multiple regression, ANN, and ANFIS models." *Int. J. Rock Mech. Min. Sci.* 46 (4): 803–810. https://doi.org/10.1016/j.ijrmms.2008.09.002.

Yin, Q., R. C. Liu, H. W. Jing, H. J. Su, L. Y. Yu, and L. X. He. 2019. "Experimental study of nonlinear flow behaviors through fractured rock samples after high-temperature exposure." *Rock Mech. Rock Eng.* 52 (9): 2963–2983. https://doi.org/10.1007/s00603-019-1741-0.

Yin, Q., G. Ma, H. Jing, H. Wang, H. Su, Y. Wang, and R. Liu. 2017. "Hydraulic properties of 3D rough-walled fractures during shearing: An experimental study." *J. Hydrol.* 555: 169–184. https://doi.org/10.1016/j.jhydrol.2017.10.019.

Yin, T. B., X. B. Li, W. Z. Cao, and K. W. Xia. 2015. "Effects of thermal treatment on tensile strength of Laurentian granite using Brazilian test." *Rock Mech. Rock Eng.* 48 (6): 2213–2223. https://doi.org/10.1007/s00603-015-0712-3.

Zhang, L. Y., X. B. Mao, M. Li, B. Li, R. X. Liu, and A. H. Lu. 2020. "Brittle–ductile transition of mudstone in coal measure rock strata under high temperature." *Int. J. Geomech.* 20 (1): 04019149. https://doi.org/10.1061/(ASCE)GM.1943-5622.0001549.

Zhang, Q. B., and J. Zhao. 2013. "Determination of mechanical properties and full-field strain measurements of rock material under dynamic loads." *Int. J. Rock Mech. Min. Sci.* 60 (8): 423–439. https://doi.org/10.1016/j.ijrmms.2013.01.005.

Zhang, Q. B., and J. Zhao. 2014. "A review of dynamic experimental techniques and mechanical behaviour of rock materials." *Rock Mech. Rock Eng.* 47 (4): 1411–1478. https://doi.org/10.1007/s00603-013-0463-y.

Zhou, T., and J. B. Zhu. 2017. "An experimental investigation of tensile fracturing behavior of natural and artificial rocks in static and dynamic Brazilian disc tests." *Procedia Eng.* 191: 992–998. https://doi.org/10.1016/j.proeng.2017.05.271.

Zhou, W., X. Y. Shi, X. Lu, C. C. Qi, B. Y. Luan, and F. M. Liu. 2020. "The mechanical and microstructural properties of refuse mudstone-GGBS-red mud based geopolymer composites made with sand." *Constr. Build Mater.* 253: 119193. https://doi.org/10.1016/j.conbuildmat.2020.119193.

Zhou, Y. X., K. Xia, X. B. Li, H. B. Li, and F. Dai. 2012. "Suggested methods for determining the dynamic strength parameters and mode-I fracture toughness of rock materials." *Int. J. Rock Mech. Min. Sci.* 49: 105–112. https://doi.org/10.1016/j.ijrmms.2011.10.004.

Zhou, Z. L., X. Cai, D. Ma, L. Chen, S. Wang, and L. Tan. 2018. "Dynamic tensile properties of sandstone subjected to wetting and drying cycles." *Constr. Build Mater.* 182: 215–232. https://doi.org/10.1016/j.conbuildmat.2018.06.056.

Zhu, W. C., and C. A. Tang. 2006. "Numerical simulation of Brazilian disk rock failure under static and dynamic loading." *Int. J. Rock Mech. Min. Sci.* 43 (2): 236–252. https://doi.org/10.1016/j.ijrmms.2005.06.008.

Zuo, J. P., H. Xie, H. Zhou, and S. Peng. 2007. "Thermal–mechanical coupled effect on fracture mechanism and plastic characteristics of sandstone." *Sci. China Ser. E: Technol. Sci.* 50: 833–843. https://doi.org/10.1007/s11431-007-0081-6.